

# The assembly, characterization, and performance of SISTINE

Nicholas Nell<sup>a</sup>, Kevin France<sup>a</sup>, Nicholas Kruczek<sup>a</sup>, Brian Fleming<sup>a</sup>, Stefan Ulrich<sup>a</sup>, Patrick Behr<sup>a</sup>, Manuel A. Quijada<sup>b</sup>, Javier Del Hoyo<sup>b</sup>, John Hennessy<sup>c</sup>

<sup>a</sup>University of Colorado, Laboratory for Atmospheric and Space Physics, 1234 Innovation Drive, Boulder, Colorado 80303, United States

<sup>b</sup>NASA Goddard Space Flight Center, Code 551, Greenbelt, MD 20771

<sup>c</sup>Jet Propulsion Laboratory, California Institute of Technology, 4800 Oak Grove Drive, Pasadena, CA, USA 91109

**Abstract.** The Suborbital Imaging Spectrograph for Transition region Irradiance from Nearby Exoplanet host stars (SISTINE) is a rocket-borne ultraviolet (UV) imaging spectrograph designed to probe the radiation environment of nearby stars. SISTINE operates over a bandpass of 98 – 127 and 130 – 158 nm, capturing a broad suite of emission lines tracing the full  $10^4 - 10^5$  K formation temperature range critical for reconstructing the full UV radiation field incident on planets orbiting solar-type stars. SISTINE serves as a platform for key technology developments for future ultraviolet observatories. SISTINE operates at moderate resolving power ( $R \sim 1500$ ) while providing spectral imaging over an angular extent of  $\sim 6'$ , with  $\sim 2''$  resolution at the slit center. The instrument is composed of an  $f/14$  Cassegrain telescope that feeds a  $2.1\times$  magnifying spectrograph, utilizing a blazed holographically ruled diffraction grating and a powered fold mirror. Spectra are captured on a large format microchannel plate (MCP) detector consisting of two  $113 \times 42$  mm segments each read out by a cross delay-line anode. Several novel technologies are employed in SISTINE to advance their technical maturity in support of future NASA UV/optical astronomy missions. These include enhanced aluminum lithium fluoride coatings (eLiF), atomic layer deposition (ALD) protective optical coatings, and ALD processed large format MCPs. SISTINE was launched a total of three times with two of the three launches successfully observing targets Procyon A and  $\alpha$  Centauri A and B.

**Keywords:** ultraviolet, sounding rocket, spectrograph.

## 1 Introduction

SISTINE is a rocket-borne far-ultraviolet (FUV; 91.2 – 180 nm) spectrograph previously described in Refs. 1 and 2. This paper focuses on the implementation of SISTINE and describes assembly, characterization, and laboratory and flight performance of the instrument. Technology development efforts and results for SISTINE are discussed. Characterization of the instrument and the facilities that allow complete in-band characterization of the instrument are described. SISTINE was launched a total of three times, two flights of which successfully acquired target data. The final flight of SISTINE notably launched from the Arnhem Space Center in the Northern Territory, Australia, allowing observation of a Southern target,  $\alpha$  Centauri A+B. Descriptions of modifications and improvements made to the instrument between flights are summarized. We describe the final flight performance of the instrument, demonstrating the capabilities of SISTINE to probe the FUV radiation environments of nearby stars and mature key optical technologies now planned for adoption by larger NASA astrophysics missions.

## 2 SISTINE Science Objectives

Characterization of exoplanet atmospheres, including the potential for habitability, requires an understanding of the interaction with the host star's UV radiation environment.<sup>3-5</sup> F, G, K, and M type dwarf stars (approximately 20 - 0.1 solar masses) are hosts to Earth-mass planets located in habitable zones. Many of these systems will be searched for biomarkers by NASA's large missions

including the James Webb Space Telescope (JWST) and the upcoming Habitable Worlds Observatory (HWO). FUV radiation impacts chemicals such as  $\text{H}_2\text{O}$ ,  $\text{CO}_2$ , and  $\text{CH}_4$ . The host star's  $\text{Ly}\alpha$  is a significant contributor to these effects and can also be used as a proxy for the extreme-ultraviolet (EUV; 10 – 91.2 nm) flux from the host star.<sup>6</sup> EUV flux is likely to have a significant effect on atmospheric mass loss on exoplanets but is difficult to measure directly due to attenuation by the interstellar medium (ISM). Additionally, flare activity in the FUV can be correlated to large ejections of charged particles that can heavily affect  $\text{O}_3$  quantity in an atmosphere.<sup>7</sup> SISTINE's imaging capability and spectral resolution allow the investigation of low-mass star FUV environments and their effects on potential exoplanet atmospheres. The spatial axis imaging capability of SISTINE allows the subtraction of geocoronal  $\text{Ly}\alpha$ . With the ability to subtract the geocoronal contribution, the targeted spectral resolution of SISTINE ( $R \sim 7000$  at 121.6 nm) is intended to resolve and reconstruct the target star's  $\text{Ly}\alpha$  emission line profile.<sup>6,8</sup> SISTINE provides spectral coverage from 98 – 127 and 130 – 158 nm. This range spans strong atomic emission lines tracing various formation temperatures in the stellar atmosphere:  $10^4$  K ( $\text{Ly}\alpha$ , 121 nm),  $10^5$  K (C IV, 155 nm), and  $10^{5.5}$  K (O VI, 103 nm).

### 3 Instrument Description

#### 3.1 Instrument Design

The design of SISTINE has been modified since the descriptions in previous literature and we present the final design of SISTINE as fabricated. SISTINE is an imaging spectrograph. Target light is imaged by an  $f/14$  Cassegrain telescope with a 0.5 m diameter primary mirror onto a  $10'' \times 6'$  entrance slit. The spectrograph is composed of a concave spherical holographically ruled grating, a concave cylindrical fold mirror, and a microchannel plate (MCP) detector. This optomechanical layout is shown in Figure 1. Target light passes through the entrance slit, is dispersed by the grating, reflected off of the fold mirror, and captured on the detector. The cylindrical figure of the fold mirror serves to match the tangential and sagittal foci of the grating on the focal plane, as well as reduce the linear dispersion at the focal plane maintaining the desired bandpass on the detector.

The slit jaw is angled  $45^\circ$  relative to the telescope boresight. Light that does not pass through the entrance slit is reflected off of the 36 mm diameter polished aperture surface onto an aspect camera. The aspect camera field of view is approximately  $12.5' \times 17.5'$ . The video feed from the aspect camera is monitored in real time to align the instrument to targets in flight or calibration environments. The aspect camera in SISTINE is a Photonis Nocturn XL that contains a CMOS sensor optimized for low light levels without the use of an intensifier. Commercially available optical lenses are assembled in a ruggedized lens tube to image the slit jaw focal plane onto the camera sensor.

Light that passes through the slit is incident upon the grating. The SISTINE grating is holographically ruled for a central density of 3016.6 g/mm and blazed via ion etching. The blaze angle of  $10.9^\circ$  is optimized to maximize efficiency in the -1 order at a wavelength of 120 nm. The grating is mounted with a  $4.6 \pm 0.1^\circ$  tilt such that zero order light is directed towards a light trap and light from the -1 order is directed towards the fold mirror and reflected onto the detector. Details on the grating, fold, and detector are provided in Table 1. This design results in an average dispersion of 0.256 nm/mm at the detector. Because the detector is composed of two separate segments there is a small unimaged gap in the center of the spectrum resulting in a bandpass of 98 – 127 and 130 –

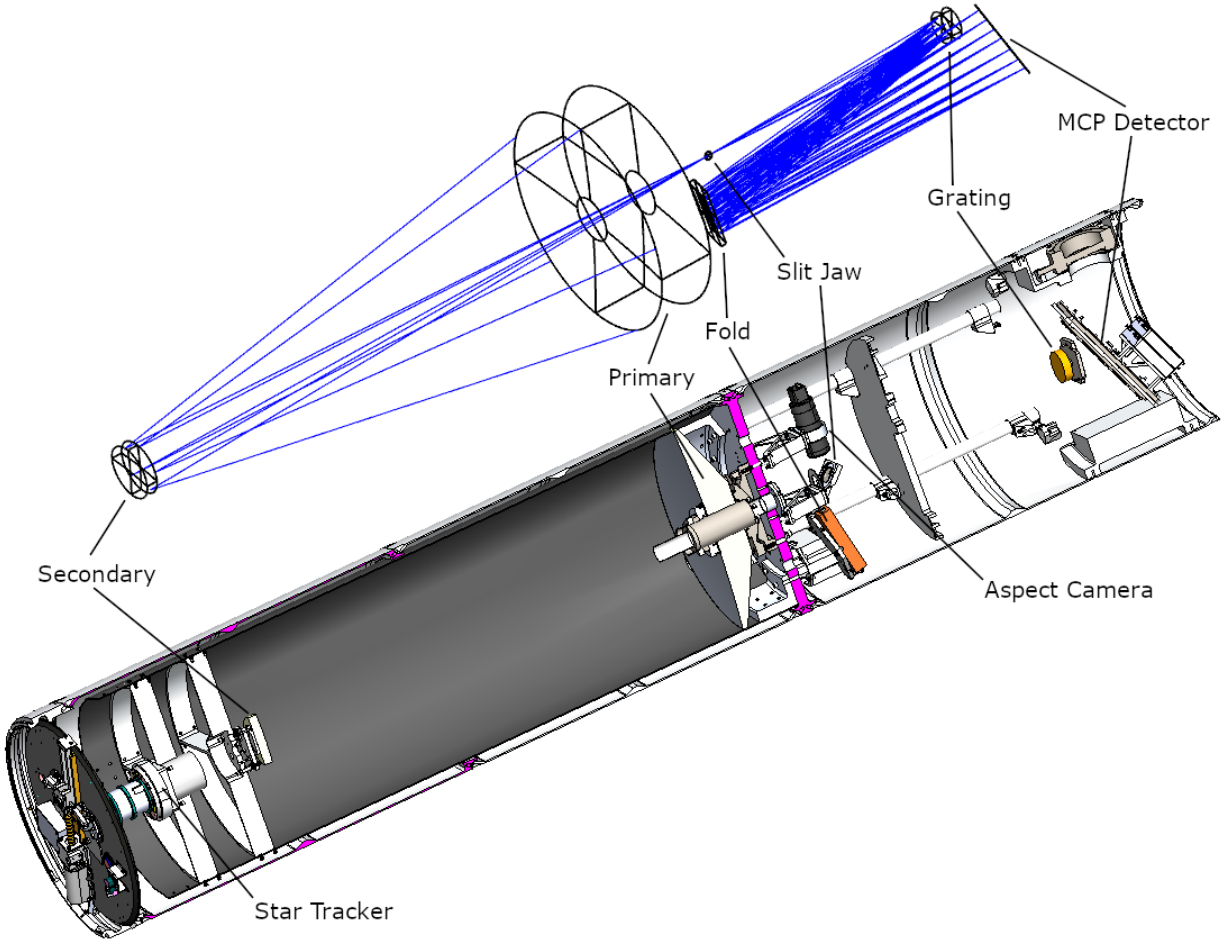


Fig 1: The SISTINE optical raytrace (upper) and mechanical CAD (lower) layouts are shown. Light enters the system on the left side of the image. The star tracker, used to acquire attitude and maintain low jitter during flight, is located in the telescope aperture and coupled to the optical metering structure. The aspect camera that images the slit jaw and allows fine pointing maneuvers in flight is shown near the center of the system. The spectrograph MCP detector is located on the right side of the image and is the focal plane responsible for capturing spectra.

158 nm. The spectrograph optical system is  $\sim f/29.4$  and thus magnifies the point spread function (PSF) imaged from the telescope focal plane by a factor of  $\sim 2.1$  on the detector. This results in a PSF FWHM size incident upon the detector of  $\sim 40 \mu\text{m}$  (without factoring in spectrograph aberrations). The specified detector resolution element ( $40 \mu\text{m}$  FWHM) is matched to this PSF and results in a minimum detectable PSF FWHM size of  $\sim 63 \mu\text{m}$  when spectrograph aberrations are factored in, resulting in a resolving power of  $\sim 7400$  at 120 nm. Predicted resolving power for a  $0.6''$  FWHM telescope PSF is shown in Figure 2 for detector resolution element sizes of  $40 \mu\text{m}$  (specified) and  $62 \mu\text{m}$  (empirical).

SISTINE employs a large format MCP detector designed and fabricated by Sensor Sciences LLC. It is composed of two independent segments each with an active area of  $113 \times 42 \text{ mm}$ . A gap of  $\sim 11.7 \text{ mm}$  exists between the two segments where light is not detected. Each segment is a “Z” format stack of three borosilicate atomic layer deposition (ALD) processed microchannel plates with  $20 \mu\text{m}$  pores and a  $13^\circ$  bias angle. The pore bias angle is aligned along the instrument

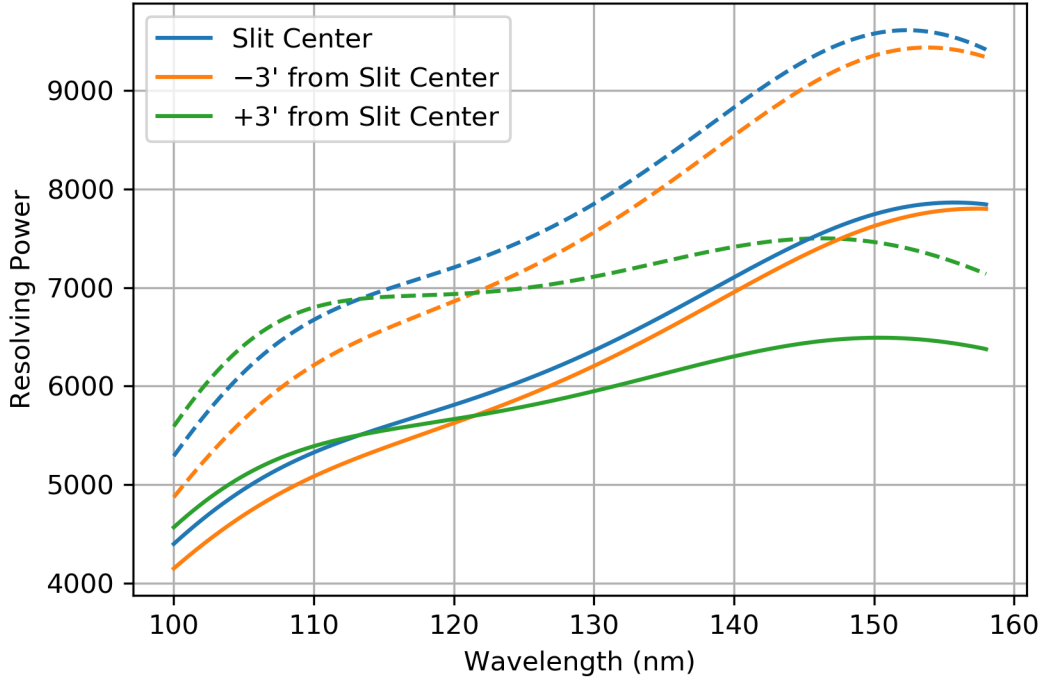


Fig 2: Modeled SISTINE resolving power for a telescope design with a 0.6" FWHM PSF. Dashed lines correspond to a detector resolution element size of 40  $\mu\text{m}$  (specified) and solid lines correspond to a detector resolution element size of 62  $\mu\text{m}$  (empirical). Resolving power is shown at three points across the imaging axis, at the center of the slit and at either end of the slit.

cross dispersion axis. An opaque cesium iodide (CsI) photocathode was deposited on the upper plate of each segment. Each segment is read out by a cross delay line (XDL) anode with anode delays of  $\sim 69$  ns in the X axis and  $\sim 49$  ns in the Y axis. Digitization in both spatial axes is comprised of 14 bits, pulse height is digitized with 10 bits with a full photon position and pulse height encoded in 38 bits.

The instrument electronics section contains the readout electronics for the detector, high voltage power supplies to bias the detector MCPs, instrument control electronics, analog signal conditioning, a vacuum gauge, and a telemetry interface to format detector data for downlink. A block diagram of these subsystems is shown in Figure 3. A power conditioning board powers all of these subsystems from a single 28 V battery pack located in the telemetry section built by the NASA Sounding Rocket Operations Contract (NSROC) engineers. An instrument control board reads uplink and timer signals from the telemetry section (TM) and allows real time control of the high voltage (HV) biasing, aspect camera alignment LED, and reset of the telemetry interface (TMIF). The control board also monitors payload pressure and instrument status and passes that data to the TM for downlink. Thermistor voltages, instrument voltages, and instrument currents are conditioned by the analog signal conditioning board and passed to a WFF93 analog deck that digitizes those values and telemeters them for real time monitoring during flight and testing. Analog detector data from each segment is amplified by a pair of preamplifiers located close to the detector in the spectrograph section. The amplified signals are transmitted to a pair of time to digital converters (TDC) with the end of each anode signal being passed through an appropriate delay line

Table 1: SISTINE instrument design summary.

Telescope	
Geometric Collecting Area	1830 cm <sup>2</sup>
Focal Length	7000 mm
Field of View	12.5' × 17.5'
Primary Diameter	500 mm
Primary Radius	3000 mm
Primary Conic	-1.0
Secondary Diameter	120 mm
Secondary Radius	810.22 mm
Secondary Conic	-2.388
Spectrograph	
Bandpass	98 – 127, 130 – 158 nm
Spectral Resolving Power	~ 2000
Entrance Slit	10'' × 6'
Grating Diameter	75 mm
Grating Radius	850.39 mm
Grating Ruling Density	3016.6 g/mm
Grating Blaze Angle	10.9°
Fold Dimensions	165 × 50 mm
Fold Radius	7000 mm
Detector	
Active Segment Size	113 × 42 mm
Spectral Axis Resolution Element	62 μm
Pore Size	20 μm
Pore Bias Angle	13°

to match the anode delay.<sup>9</sup> The TDCs digitize these analog signals and output ethernet packets containing X position, Y position, and a pulse height for each photon. Ethernet from each TDC is routed to a ruggedized commercial gigabit ethernet switch and data from the switch is routed to the TMIF. The TMIF parses all of this data, performs minor encoding, and outputs data in a synchronous parallel format to a WFF93 parallel deck in the TM section. This system enables real time monitoring of detector data during testing and flight.

### 3.2 Technology Development

SISTINE is used as a platform for the maturation of novel technologies relevant to astrophysical applications in the FUV. These technologies are ALD processed borosilicate MCPs with large formats, enhanced lithium fluoride (eLiF) optical coatings tailored to the FUV, and environmentally protective ALD optical coatings. Borosilicate MCPs allow larger format detectors to be built and ALD processing of the MCPs allows control of gain and MCP resistance. While Al+LiF mirrors have been used successfully on several past missions the eLiF effort focuses on improving the quality of the LiF layer by optimizing the temperature of the substrate. Finally, efforts to protect

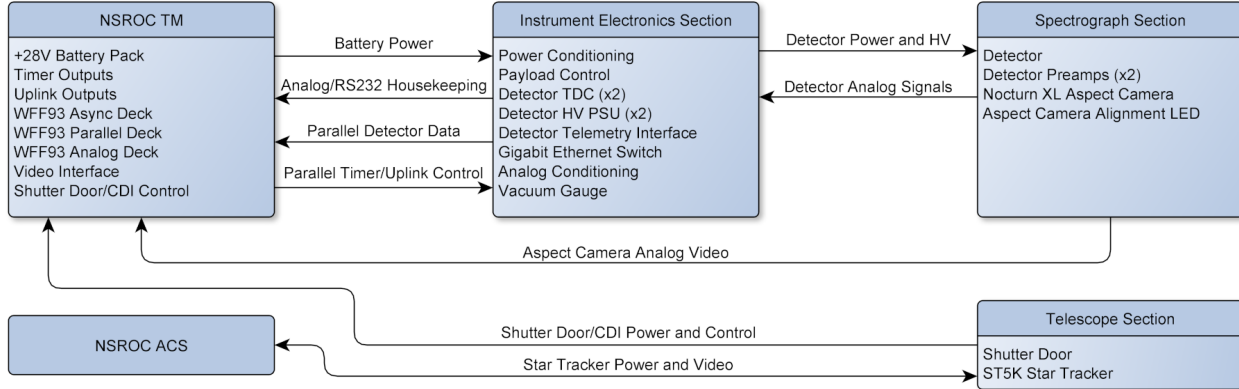


Fig 3: Electrical system block diagram of the SISTINE payload. Instrument electronics are hermetically isolated from the telescope and spectrograph sections. Critical data paths are shown as directional connections between the various blocks.

the LiF layer with a final thin “capping” layer of a protective material with sufficient transmissivity is carried out via ALD. These efforts are discussed in detail in the following two sections.

### 3.2.1 Large format MCP detectors

ALD processed borosilicate MCPs are available in formats up to  $200 \times 200$  mm and these types of plates are shown to have better gain stability than traditional plates.<sup>10–14</sup> This work builds upon the state of the art detectors flown on FUSE and HST-COS which both used segment sizes of  $85 \times 10$  mm and each employed two segments. SISTINE has segment sizes of  $113 \times 42$  mm and also employs two segments with an XDL readout for each segment. Resolution elements of  $62 \mu\text{m}$  along the X axis and  $38.5 \mu\text{m}$  along the Y axis were achieved with the SISTINE detector characterized via pinhole mask testing performed at Sensor Sciences LLC. The SISTINE detector with photocathode applied is shown in Figure 4. An opaque CsI photocathode was applied to the top surface of each MCP stack, resulting in detector efficiency performance comparable to that of HST-COS<sup>15</sup> and GOLD<sup>16</sup> and efficiency measurements are provided in Section 4.2.

The SISTINE detector employs recent advances in MCP technology, ALD processed MCPs made of borosilicate substrates. A notable aspect of this detector is the large active area, a total of  $94.92 \text{ cm}^2$ , made possible by advances in MCP fabrication technology. The MCPs for the SISTINE detector were fabricated by Incom, who have pioneered the development of the borosilicate MCP substrate.<sup>14</sup> These MCPs have resistance and secondary emission characteristics driven by ALD. The ALD processed borosilicate MCPs allow for the fabrication of large formats with improved gain stability and lifetime while maintaining low background rates.<sup>10–13</sup> Only basic functional testing was performed at the Laboratory for Atmospheric and Space Physics (LASP) prior to detector installation in SISTINE. Throughout the course of SISTINE testing and flight, no notable changes were observed in detector behavior. This detector was refurbished and new photocathodes were deposited between the first and second SISTINE flights in September, 2020.

### 3.2.2 Enhanced protective optical coatings for the FUV

Efforts to improve the reflectivity of aluminum coated optics in the FUV have been employed on multiple optics in SISTINE through the use of eLiF and an ALD protective coating.<sup>17,18</sup> While Al+LiF has been deposited and flown successfully on FUSE it is known that Al+LiF mirrors are

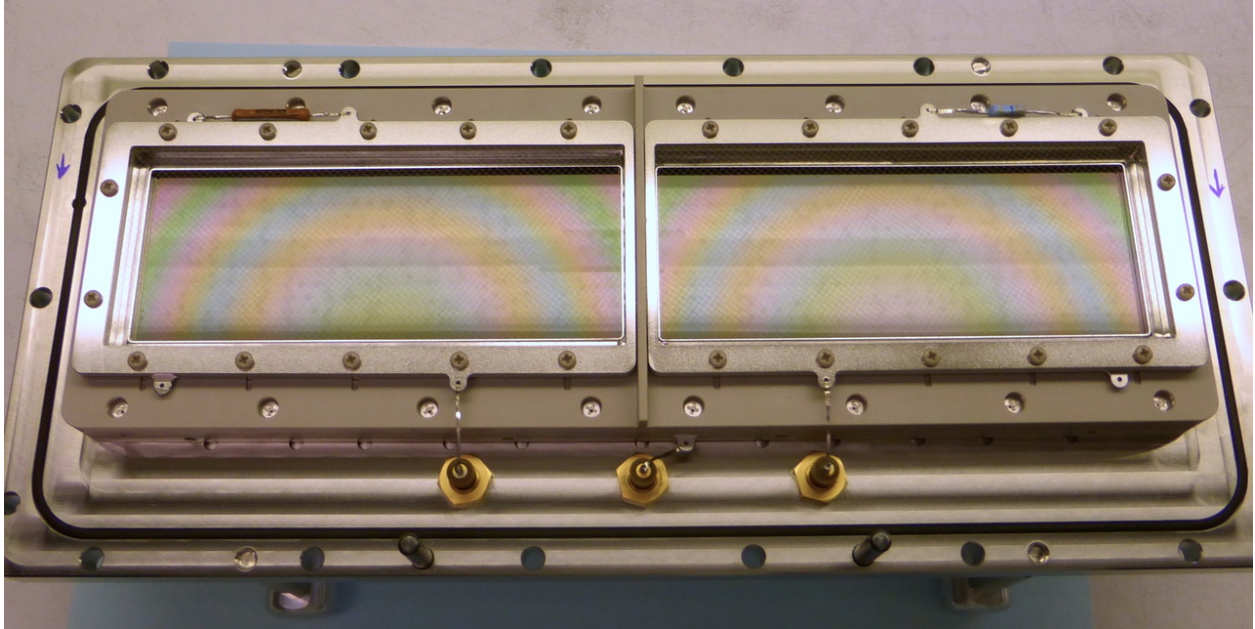


Fig 4: The fully assembled SISTINE MCP detector. The shorter wavelengths fall on the left segment and longer wavelengths fall on the right segment. Each segment is  $113 \times 42$  mm. Minor thickness variations in the CsI photocathode are responsible for the fringing effect visible on each segment. A QE enhancement grid is visible oriented in a rotation roughly  $45^\circ$  off of the primary segment axes.

sensitive to humidity and can suffer reflectivity degradation over time when exposed to environments with sufficient humidity.<sup>19</sup> The eLiF technology development effort has focused on improving reflectivity in the FUV and simultaneously improving the environmental stability of the coated mirrors. The eLiF effort employs elevated substrate temperatures with the goal of lowering the extinction coefficient of the LiF layer. Evaporated LiF has been shown to have a significantly higher extinction coefficient than crystalline LiF at short wavelengths which is undesirable for high reflectivity coatings.<sup>20</sup> In addition, the ALD technology development focuses on protecting the LiF layer, deposited via physical vapor deposition, with a final layer of another more environmentally resistant material deposited via ALD.<sup>21</sup> Three optics in SISTINE were coated with Al+eLiF, the primary mirror, secondary mirror, and fold mirror. The secondary mirror was also coated with a capping layer of  $\text{AlF}_3$  via ALD.<sup>21</sup> We note that the grating flown on SISTINE is a replica and thus was not able to be coated with eLiF due to the material properties of the replica not being compatible with the substrate temperatures required for eLiF deposition. Replica gratings are produced using an epoxy layer on the replica substrate to generate a high fidelity copy of the originally fabricated master grating.<sup>22</sup> Discussions with the grating vendor, Horiba Jobin-Yvon, concluded that the epoxy used in their replication process is not compatible with the high substrate temperatures required for eLiF deposition. Deposition of eLiF is performed via physical vapor deposition but the optical substrate is brought up to a temperature of approximately  $250^\circ\text{C}$  prior to deposition to improve packing density of the LiF, thus reducing porosity and surface roughness. All optical substrates for SISTINE were radiatively heated with infrared lamps with a proxy sample used to estimate temperature of the optical substrate. The secondary and fold mirrors both showed improved reflectivity while the primary mirror did not show notable improvement over ambient temperature

LiF deposition. The primary mirror has a significantly larger volume than the secondary or fold mirrors making it extremely difficult to heat uniformly at high temperatures in a vacuum environment to achieve the desired substrate temperature for deposition.<sup>23</sup> We note that it was not possible to measure the SISTINE primary mirror directly due to the size and mass of that mirror so all results for the primary mirror are inferred from the witness sample which was closely thermally coupled to the primary mirror via a hub mount located in the central cutout of the primary mirror during the coating process. Details of handling and storage of the optics and witness samples is explained in Section 4.2.

It is also notable that witness samples for the secondary and fold mirrors had higher reflectivities than the optics themselves. These results implied that one of the challenges with achieving good eLiF results is controlling substrate temperature. Ultimately the best results achieved were on the secondary witness sample, shown in Figure 5, which demonstrate the potential of eLiF with peak reflectivities of 90% near 115 nm. The efficiencies observed suggest that the eLiF deposition process reduces the extinction coefficient of the LiF layer at short wavelengths but a measurement of the indices of refraction for eLiF has not yet been made. The secondary mirror and secondary witness sample were additionally coated with 10 cycles of AlF<sub>3</sub> via ALD at Jet Propulsion Laboratory to protect the LiF layer. The AlF<sub>3</sub> deposition had a minimal effect on the overall reflectivity (see Figure 5). No controlled aging studies were possible with the SISTINE optics but we show a comparison of the secondary and fold optics measured prior to installation into the SISTINE instrument and then after the three launches in Figure 6. Both optics maintained high reflectivity throughout their active usage in SISTINE and show different aging trends. Note that the aging trend seen for the secondary mirror shown in Figure 6 is qualitatively similar to the change in reflectivity seen after ambient aging for an Al+AlF<sub>3</sub> mirror sample shown in Reference 24. This appears to show that the ALD AlF<sub>3</sub> layer is serving the intended purpose and is the material primarily interacting with the environment. These results suggest that AlF<sub>3</sub> in particular may be of interest when stability at the shortest wavelengths is paramount. The ratio values shown in the lower panels of Figure 6 are only shown down to the cutoff wavelength because the extinction coefficient of evaporated LiF shows little difference to that of crystalline LiF at wavelengths short of the cutoff.<sup>20</sup> Efforts to develop high efficiency LiF coatings have continued after the SISTINE results and are discussed in Refs. 23 and 25.

### 3.3 Mechanical Design

SISTINE is an aft-looking payload housed in 22” hermetic aluminum skins. There are three distinct mechanical sections, the telescope, the spectrograph, and the electronics (see Figure 7). The telescope and spectrograph sections are a single hermetic manifold that can be pumped through a valved port to achieve low pressures ( $< 1 \times 10^{-5}$  Torr) where the detector can be operated for testing. The hermetic section also allows the payload to be filled with nitrogen to keep the optics and detector safe during shipment or down time when the payload cannot be actively pumped. The telescope aperture is closed with a hermetic shutter door designed and fabricated by NSROC. The electronics section is built on a bulkhead that seals the other end of the telescope and spectrograph hermetic manifold.

The optical system is metered off of a single central bulkhead located between the telescope and spectrograph sections (see Figure 7). This mounting scheme attempts to mitigate thermal effects from the rapid heating of the outer aluminum skins during ascent through the atmosphere. The



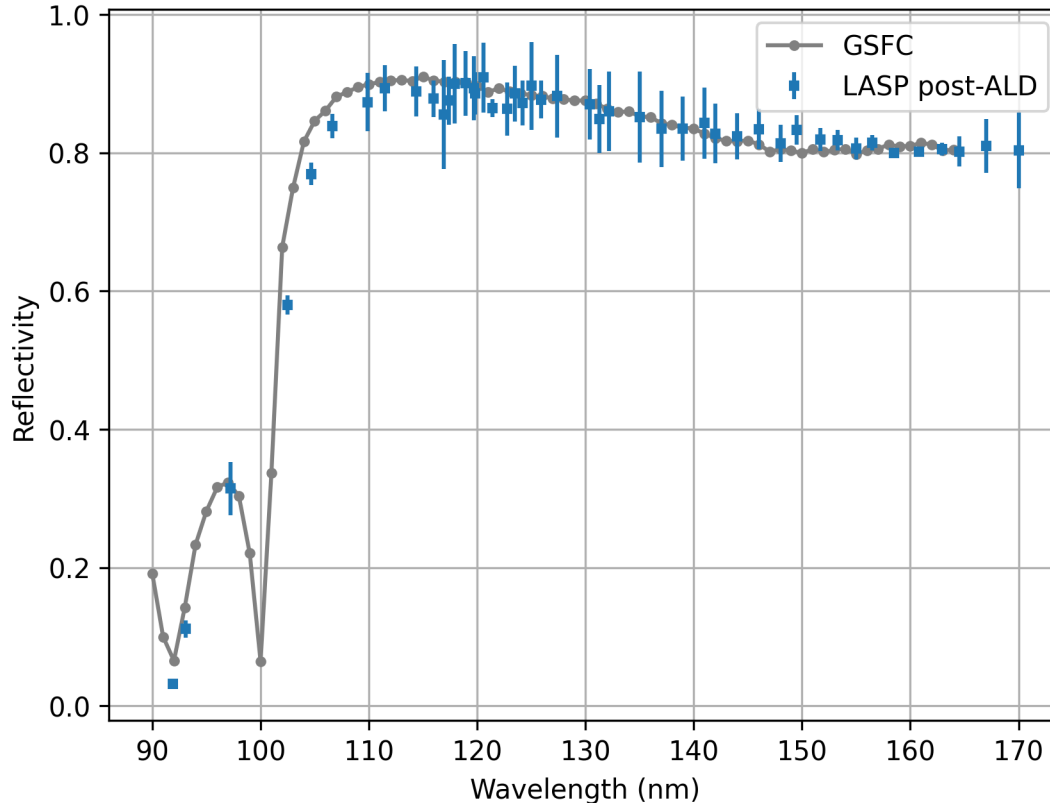


Fig 5: Reflectivity measurements of the SISTINE secondary mirror witness sample measured after deposition of Al+eLiF at GSFC (grey points) and after ALD  $\text{AlF}_3$  coating (blue points). Data shown in grey are measurements performed by GSFC and data shown in blue are measurements performed by LASP. The  $\text{AlF}_3$  ALD coating has only a minor effect on the overall reflectivity of the sample most pronounced at the LiF cutoff wavelengths near 102 nm. This sample was the best demonstration of the capability of eLiF with peak reflectivities of 90% near 115 nm.

telescope and spectrograph metering sections are independent fabrications and employ different designs suited to each application. The spectrograph metering structure is an open frame with aluminum decks for optical mounts. This structure allows access to spectrograph optical components to facilitate optical alignment.

## 4 Instrument Assembly and Characterization

### 4.1 Characterization Facilities

Component and instrument characterization in-band occurs in two facilities at LASP. Component characterization is performed in the “square tank”, originally described in Ref. 26 and used to measure optical constants for a wide variety of coating materials in the EUV and FUV.<sup>27,28</sup> Since that time the facility has undergone some changes and a more recent description is contained in Ref. 29. The chamber and sample manipulation stages retain nearly identical functionality and have some modularity to be used for normal or grazing incidence measurements as well as having the capability to accommodate different grating measurements. Two monochromators are used to illuminate samples, a McPherson 310 is used for wavelengths spanning 1 – 121.6 nm and an Acton

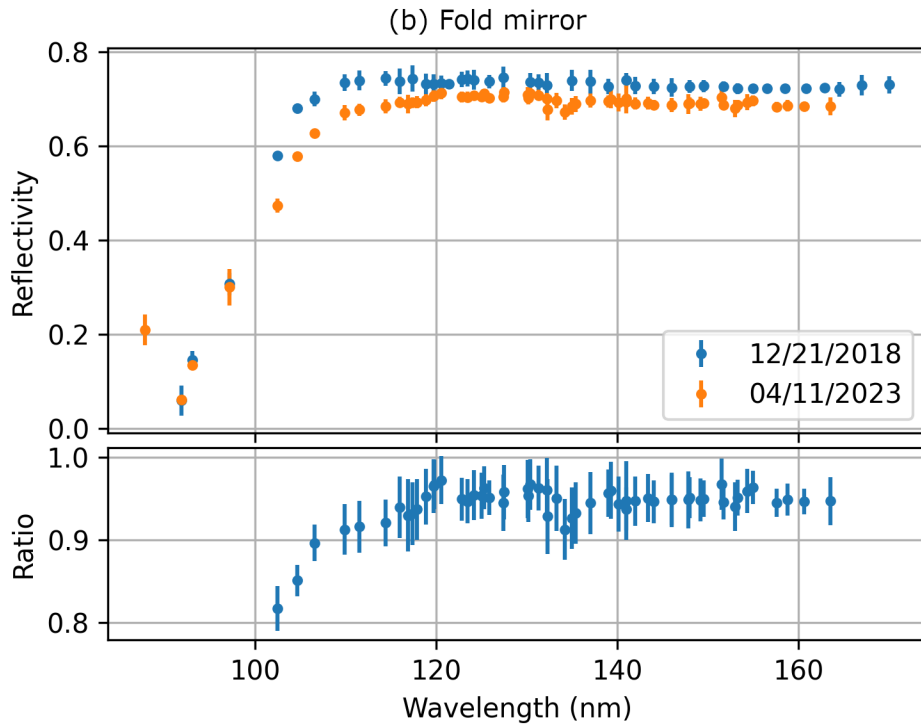
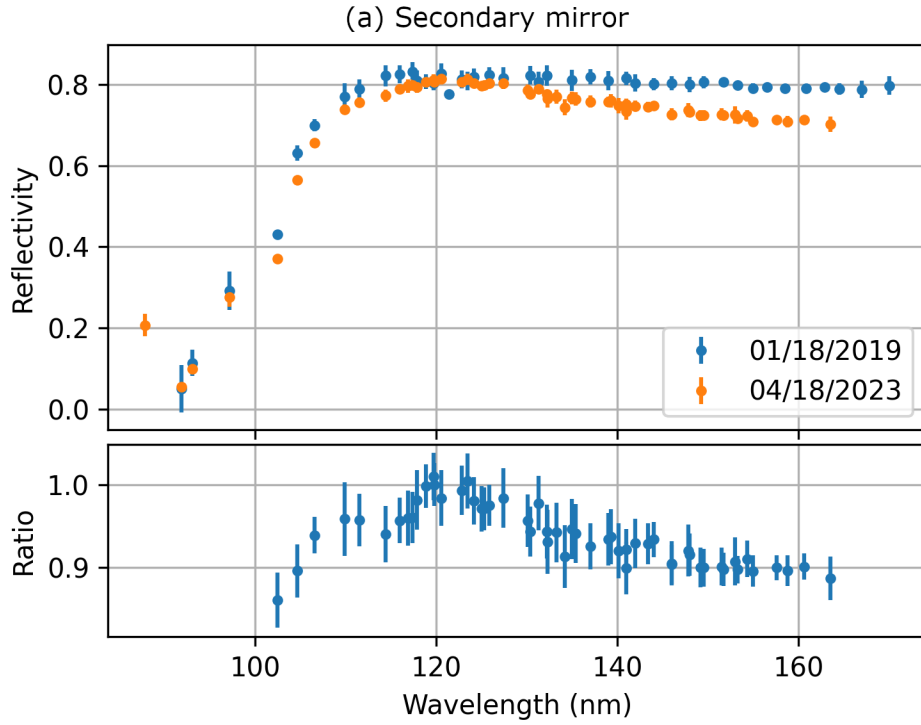


Fig 6: Reflectivity measurements for the secondary (a) and fold (b) mirrors from before installation into the payload and after the final flight of SISTINE are shown. The lower panels show the relative change from initial to final measurements. These measurements provide an empirical instrument usage case demonstration of performance over time for these two coating prescriptions.

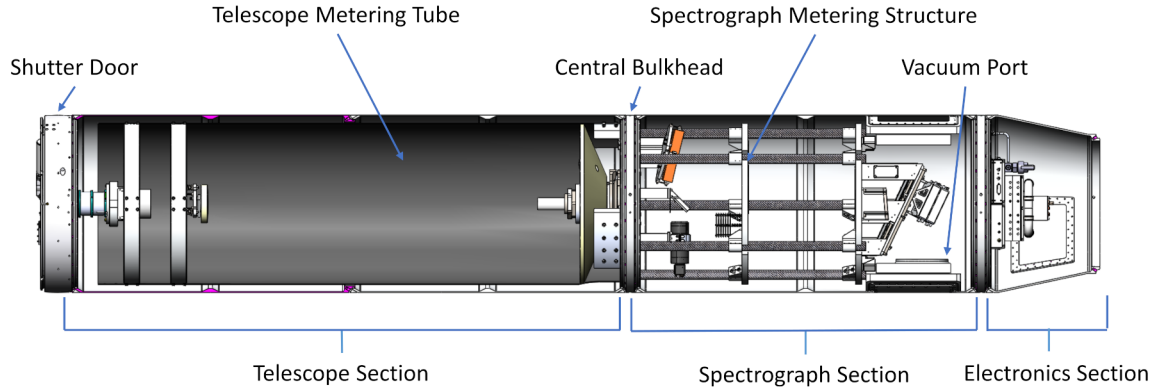


Fig 7: Mechanical layout of the SISTINE instrument. The telescope and spectrograph sections are a single hermetic manifold. All optomechanical structures are metered off of the central bulkhead. Optical metering for both the telescope and spectrograph is accomplished with carbon fiber parts. A large vacuum pump port is located in the spectrograph section allowing the entire system to reach high vacuum for testing in the laboratory.

VM-502 is used for wavelengths spanning 90 – 200 nm. It is possible to make measurements all the way through 550 nm but in practice this is much less efficient than using commercial spectrophotometers that can measure down to  $\sim 185$  nm. Three light sources are commonly used for measurements in this chamber, a Manson Model 2 soft x-ray source, a windowless hollow cathode discharge lamp,<sup>30</sup> and a Hamamatsu L9841 deuterium lamp with an  $\text{MgF}_2$  window. Two detectors are commonly used to measure across this full bandpass. An open faced MCP detector with an XDL anode and opaque CsI photocathode from Sensor Sciences LLC is used to measure shorter wavelengths. This detector uses a hybrid ALD and traditional MCP stack to achieve high gain stability despite repeated illumination in a small area. For longer wavelengths a Hamamatsu R6836 photomultiplier tube (PMT) is used. This PMT has an  $\text{MgF}_2$  window and a CsTe photocathode and is used for measurements of wavelengths spanning 115 – 300 nm. An annotated photograph of this facility is shown in Figure 8.

End-to-end instrument characterization is performed in the “long tank” chamber, originally described in Ref. 31. The “long tank” is a 23 foot long cylindrical vacuum chamber with a 30 inch inner diameter accommodating an entire sounding rocket payload within the vacuum manifold. One end of the tank contains a Newtonian collimator with a 24 inch  $f/4$  mirror. The collimator optics are coated with gold and illuminated using a windowless hollow cathode discharge lamp mounted on a stage on the side of the chamber allowing fine field position and focus adjustment. The angular size of the source is set with an interchangeable pinhole or mask at the focal plane of the collimator allowing different field illuminations to be used including a series of point sources (see Section 4.4). The instrument is optically aligned to the tank in tip and tilt using a manual stage near the chamber door. Fine adjustments are then made using the light source adjustment stage to sample different positions across the slit.

#### 4.2 Instrument Component Performance

The expected performance of the SISTINE instrument is modeled from measurements of the various components of the system. Predictions for SISTINE efficiencies and effective area were published in 2016.<sup>2</sup> Coating prescriptions are discussed in Section 3.2.2 and the detector photocath-

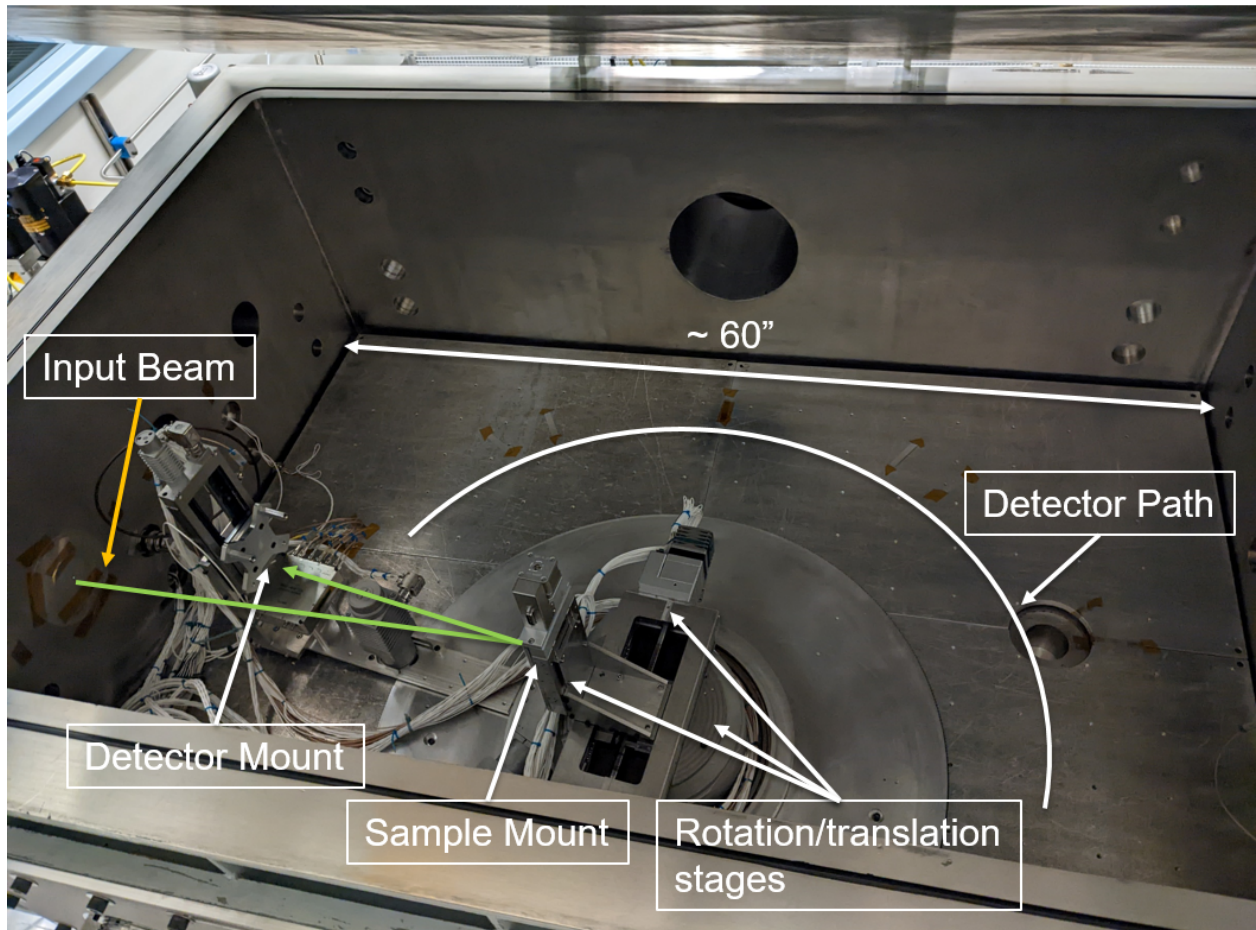


Fig 8: Annotated photograph of the square tank showing sample manipulation stages, sample and detector mounts, input beam path, and detector path. The configuration shown is typical for reflectivity measurements with the detector shown in the reflected beam measurement position. The incident beam is measured by the same detector which travels along the detector path with the sample moved out of the optical path via the sample manipulation stages. This system allows reflectivity to be measured by a single detector. A similar configuration is used for grating efficiency testing.

ode and measurements are discussed in Section 3.2.1. All of the SISTINE optics and all witness samples underwent final characterization in the LASP square tank facility, except for the primary mirror which is too large to be tested in the square tank. The estimate for the reflectivity of the primary mirror is derived from the witness sample that was coated with the primary mirror. The flight grating efficiency was tested in the same geometric configuration as used in SISTINE but a  $\sim 1$  cm circular portion near the center of the grating was illuminated for this testing. For flight optics only one measurement position is shown, but several measurements are taken across the surface to verify consistent performance across the optical surface. Results from these tests are shown in Figure 9 and are used to estimate the effective area shown in the lower panel of Figure 9.

All optics and associated witness samples were transported in hermetic containers backfilled with  $N_2$  to maintain a low humidity environment during transport. Prior to installation in the payload all optics were stored in an active  $N_2$  purge cabinet in a clean room. During all processes

witness samples are maintained in close proximity with their corresponding optics to track any potential issues during such activities and no efficiency issues were observed throughout all bonding procedures. In general, the witness samples for each optics are maintained in close proximity with the associated optic until final installation into the payload. When optics were installed into the payload their corresponding witness samples were left in N<sub>2</sub> active purge storage which maintains a low humidity environment. Handling of the optics only occurs in clean workspaces with care taken to avoid any types of molecular contamination of the optics or assemblies. Optics in the payload are occasionally exposed to the ambient atmosphere during buildup and testing operations. However, the payload itself is hermetic and generally kept at high vacuum when possible. During shipment operations the payload is backfilled with N<sub>2</sub> to a pressure of  $\sim 200$  Torr.

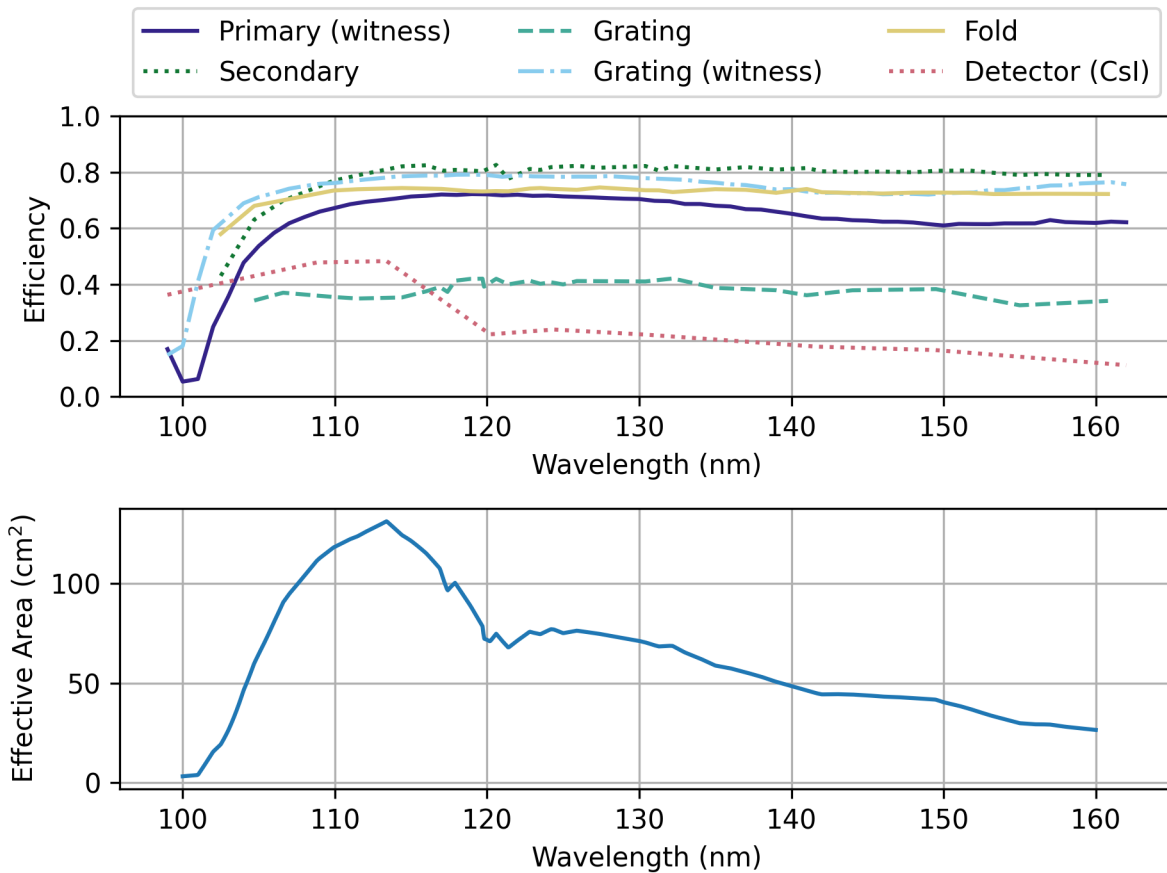


Fig 9: (Top) Efficiencies for all optical components and the detector are shown. (Bottom) The effective area of SISTINE derived from the efficiencies of the individual component is shown as a function of wavelength. Peak predicted effective area is  $\sim 120$  cm<sup>2</sup> near 115 nm.

#### 4.3 Telescope Assembly and Characterization

The entire optical system is metered off of the primary bulkhead (see Figure 7). The primary and secondary mirrors of the telescope were fabricated by Nu-Tek Precision Optics. The primary mirror is mounted directly to the primary bulkhead on a tip/tilt mount. The primary mirror is fixed in place to the mount with a threaded clamp around the inner diameter of the central cutout of the

mirror. This scheme was chosen due to the tight space constraints imposed by the mirror size and lightweighting scheme versus the available volume in a 22 inch sounding rocket manifold. After this mirror is installed, the carbon fiber (CF) telescope metering tube is attached to the primary bulkhead with large aluminum brackets. This metering tube was designed at LASP and manufactured for SISTINE by Rock West Composites. A camera is temporarily attached to the metering tube at the focal point of the SISTINE primary mirror. This subsystem is then fully illuminated with collimated light and the primary mirror is adjusted in tip and tilt to minimize the size of the PSF and remove aberrations such as coma. Once the PSF is optimized the primary mirror adjustment mechanism is locked and staked with low outgassing epoxy.

The camera is then removed from the metering tube and the secondary optic is installed on its support structure. An autocollimation test fixture is placed at the nominal telescope focal plane and the telescope is pointed at a flat reference mirror. The secondary optic is adjusted in tip, tilt, and piston to minimize the size of the PSF at the focal plane. The focal plane can be sampled both directly with a camera and indirectly with a knife edge test to measure PSF size. After the secondary mirror position is optimized, lock nuts and set screws are used to firmly hold it in place and all adjustment hardware is staked. The autocollimation test fixture is then removed and replaced with the slit jaw assembly and the aspect camera is installed.

Telescope focus prior to the first flight of SISTINE is shown in Figure 10. This focus measurement was accomplished using a light source with a wavelength of 550 nm in air. The minimum value reached is  $\sim 100 \mu\text{m}$  FWHM which is  $\sim 3''$  FWHM in angular space. We note that this measured value is the result of a double pass test where the wavefront error is doubled. The single pass PSF that would be measured in flight could therefore be as small as  $\sim 2''$  FWHM in flight. This PSF was larger than the originally targeted value of  $0.6''^2$  and was expected to have been caused by stress induced on the primary mirror from the mount. There was no time to investigate this issue during the assembly of SISTINE 1. During the SISTINE 1 flight, the mirror was found to have come loose in its mount, no spectral data of NGC 6826 was acquired during that flight. There was no damage to the mirror, so the mount was modified to double the clamping torque applied and a lock nut was added to the primary clamping nut for future flights. The telescope was again focused in a similar manner before the flight of SISTINE 2 and results of that focus run were consistent with SISTINE 1 overall but more features were apparent in the PSF. This is believed to be due to stress induced deformation in the primary mirror from the need to increase the clamp torque. The secondary support spider was initially made of multiple segments but after the first flight a monolithic spider was fabricated to ensure no change in secondary position under flight vibration environment.

This deformation of the primary mirror was modeled using finite element analysis (FEA) with the simplified assumption that the torque was uniform azimuthally across the clamping surface against the optic (see Figure 11). Even though this analysis does not perfectly model the stress on the optic it provides the magnitude of the figure error introduced from this level of torque. The sag change from the FEA analysis was fit with Zernike polynomials and this system was modeled in Zemax OpticStudio which provided results consistent with our measurements. This work occurred in late 2019 and there was not sufficient time to redesign the primary mirror mount for future flights of SISTINE. In late 2019 the SISTINE team was working towards a July 15, 2020 launch date in Australia. Payload integration and shipment schedules only allowed a few months for instrument updates and those efforts were ultimately focused on preventing the issue experienced

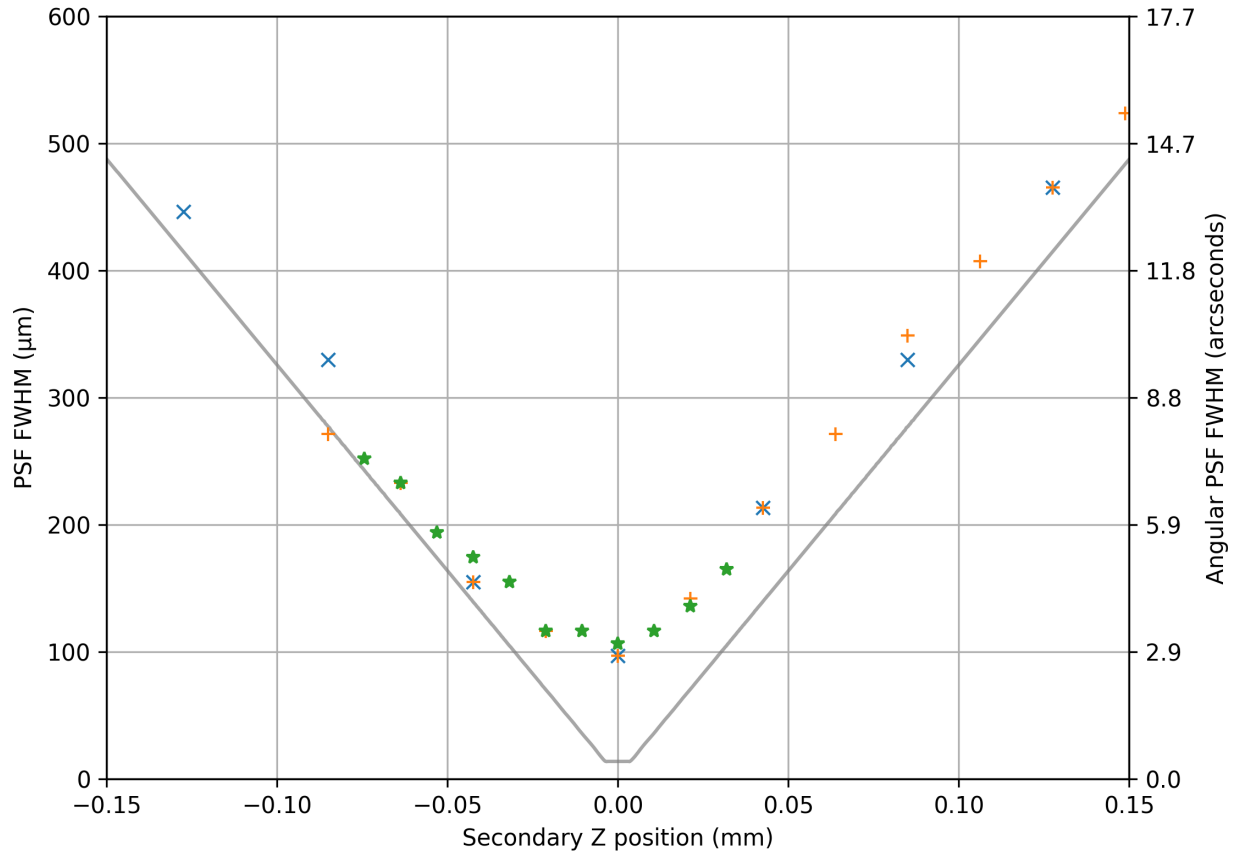


Fig 10: A double pass focus curve as a function of the secondary mirror position for the SISTINE telescope is shown. Grey lines show the theoretical focus curve as predicted with Zemax OpticStudio. Points in blue, orange, and green show measured PSF FWHM size using different step sizes.

on the SISTINE-1 launch. In early 2020 the COVID pandemic and condition of the Australia site caused an indefinite postponement of the SISTINE-2 launch date.

Between the SISTINE 2 and 3 flights, a point source microscope (PSM) similar to the design shown in Refs. 32 and 33 was fabricated and characterized for use in optical alignments. During the flight of SISTINE 2 it was observed that the telescope was out of focus and that the PSF produced by the telescope was larger than the width of the slit ( $10''$ ).<sup>34</sup> However, when the system was tested after flight, no defocus was observed. A series of tests were conducted to find the root cause of the defocus in flight, including gravity loading and thermal environment. Ultimately the thermal environment during the flight was found to have caused the defocus. The SISTINE telescope was separated from the rest of the system and placed on an optical bench in a double pass configuration with the PSM mounted on a linear stage at the focal plane such that the focus could be tracked quantitatively in real time. Industrial heat tape was applied to the exterior of the telescope skin and controlled with a variac to reproduce temperatures on the bulkhead as observed during flight. During the heating process the focus was observed to change as a function of bulkhead temperature. Once flight like temperatures were reached the distance the focus had moved in the optical axis was measured to be 3.8 mm, but at this new location the size of the PSF was still consistent with the nominal focus on SISTINE 1 and 2 as observed in the laboratory. Using the observed thermal 3.8 mm shift to predict the geometric size of the PSF results in a prediction of  $\sim$

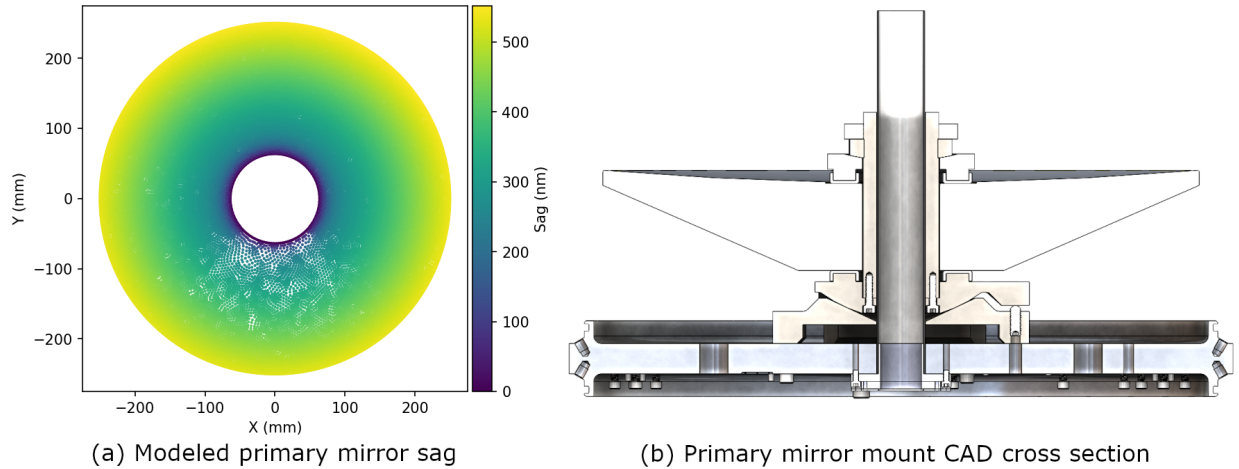


Fig 11: (a): FEA modeled primary mirror deformation from the ideal figure with a clamping torque of 154 foot pounds. (b): CAD sectional view of the SISTINE primary mirror hub mount.

27" which is consistent with the PSF size observed in flight for SISTINE 2.<sup>34</sup> The primary mirror is the optic in the telescope optical path with the most thermal coupling to the central bulkhead which experiences a significant temperature increase ( $\sim 15\text{ }^{\circ}\text{C}$ ) during vehicle ascent. Again, there was no time to redesign a primary mirror mount and the schedule for SISTINE 3 laboratory work was abbreviated due to the constraints of testing and shipment for an international campaign. Therefore, to mitigate this defocus effect for flight, the telescope was purposefully defocused by 3.8 mm in the opposite direction of the empirically determined thermally induced focus shift by adjustment of the piston position of the secondary mirror. The system was thermally tested again and the results of this solution were found to be consistent with previous laboratory focus results. SISTINE 3 successfully acquired data from  $\alpha$  Cen A+B demonstrating an in-flight PSF consistent with that measured in the laboratory<sup>35</sup> demonstrating that the thermal characterization and executed solution operated as intended (see Section 5).

#### 4.4 Spectrograph Assembly and Characterization

The spectrograph is built on the opposite side of the primary bulkhead from the telescope. A space frame was built to meter the spectrograph grating and detector. The design is based on the space frame from the Colorado High-resolution Echelle Stellar Spectrograph which had been flight proven and shown to be well suited to the sounding rocket environment.<sup>36,37</sup> The grating was fabricated by Horiba JY and the fold mirror was fabricated by Rainbow Research Optics. The fold mirror and aspect camera are mounted directly to the primary bulkhead. The only adjustable optic in the spectrograph is the fold mirror which has tip, tilt, and piston adjustment to properly align the spectrum on the detector and bring it into focus. Three motorized linear actuators are used to adjust the fold mirror so that the spectrograph can be focused in real time while the entire payload is in a vacuum chamber and illuminated with collimated FUV light. Once the fold position is optimized, it is locked and staked into place and the linear actuators are removed.

In the SISTINE design, the slit is oversized and does not drive spectral resolving power of the system. This is a feature meant to ensure that all of the flux from the observed source is captured to maximize sensitivity of the system. However, due to the performance of the telescope, it was not possible to demonstrate the full capability of the spectrograph. For focusing and characterization,



a pinhole aperture was placed at the location of the slit to effectively decrease the size of the source being fed into the spectrograph. This aperture was  $35\ \mu\text{m} \times 50\ \mu\text{m}$  with the  $35\ \mu\text{m}$  portion aligned along the spectral axis. Factoring in the plate scale of the telescope, this source has an angular size of  $1'' \times 1.5''$ . All spectrograph adjustments were made with this aperture in place. Focus operations were possible with a windowless hollow cathode source but there are a limited number of lines that are useful for characterizing limiting performance of the spectrograph itself. The N I 124.3 nm line was used for a coarse focus adjustment followed by a fine focus adjustment using a deuterium lamp and a similar method to the “shotgun” approach described in Ref. 38 for FUSE. Figure 12 shows a small subset of deuterium spectra near optimal focus. Focus was optimized near 120 nm as that was the optimized wavelength of the SISTINE optical design. Several line groups in Figure 12 were fit across various fold mirror positions to determine best focus. For final characterization of performance, a source such as a PtNe hollow cathode lamp, similar to those used for wavelength calibration of HST-COS,<sup>39</sup> would have allowed detailed characterization of resolving power over the full bandpass. At the time of spectrograph assembly and characterization for SISTINE it was not possible to find a vendor willing to fabricate a PtNe hollow cathode source with an  $\text{MgF}_2$  window. While deuterium spectra provided examples of how well the spectrograph could perform, it is difficult to extract a clear characterization due to the density of lines versus the resolving power of the system. Ultimately it was possible to demonstrate that the spectrograph had significant performance margin and would be limited by the telescope PSF. Characterization of resolving power was accomplished by switching the light source to a hollow cathode lamp fed by air. Results for both the spectrograph with a specialized calibration aperture and for the full nominal system are summarized in Table 2. With the spectrograph test aperture removed the typical resolving power observed in the “long tank” near 120 nm was  $R \sim 1500$ .

Table 2: Resolving power measured with a hollow cathode lamp

Wavelength (nm)	113.3	115.3	120.0	124.3	141.1	149.4
Spectrograph	4460	4400	4280	3950	4470	5100
Full System	1570	1560	1490	1580	1700	1690

The spectrograph focus was optimized for resolving power as it was found that all imaging requirements were met when resolving power was optimized. Only the first flight of SISTINE targeted an extended object, NGC 6826, but no target data was obtained during that flight. Subsequent flights of SISTINE observed stars and all target stars had sufficient on-sky separation to be clearly resolved by SISTINE in the imaging axis. Roll positions were chosen in advance to place the long axis of the SISTINE slit along the axis of greatest separation between stars. Figure 13 shows an imaging axis test of SISTINE. A custom pinhole mask consisting of nine pinholes spaced by 0.33 mm was created for the “long tank” collimator. These pinholes were rotationally aligned with the SISTINE long slit axis to test imaging performance across  $\sim 4'$  of the imaging axis. The imaging axis maintains performance limited by the combination of the telescope and “long tank” collimator,  $\sim 2.8''$ , across the detector extent illuminated with this mask. This was the largest angular extent able to be tested without mechanical modification of the “long tank” light source aperture. The final PSF achieved with the SISTINE telescope sets the upper limit on resolving power of the system and limits the ability to reconstruct the stellar  $\text{Ly}\alpha$  profile, however, sufficient resolving

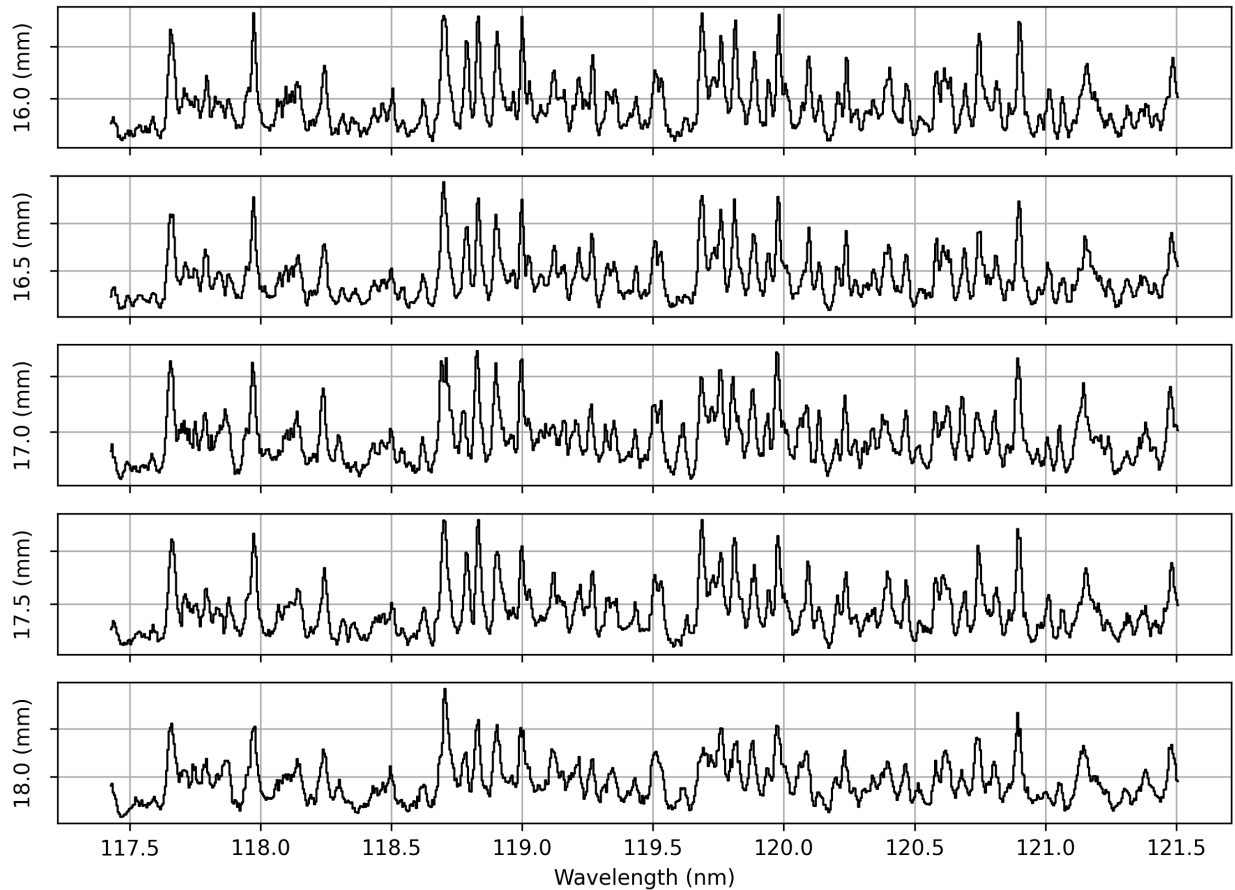


Fig 12: A set of deuterium spectra taken at different fold mirror positions. The Y axis labels show position of the fold mirror in mm along the optical axis. The intensity of each spectrum is shown in arbitrary units. The wavelength solution is approximate as each spectrum has to be positionally corrected after fold mirror positioning in post processing for comparison. Although data is taken over the full bandpass only a small subset is shown to demonstrate detail.

power is demonstrated to resolve all other emission lines throughout the SISTINE bandpass.

#### 4.5 Assembly Schedule

The timeline for the assembly, alignment, and characterization of SISTINE was heavily abbreviated. The first launch of SISTINE was targeted for mid-2019 in advance of an anticipated campaign to Australia, which at the time was scheduled for mid-2020. The SISTINE mission initiation conference was held in March of 2018. Major components such as the detector, optics, and skins were on site at LASP in late 2018 and the final optical coating was completed and measured in January of 2019. Assembly of the instrument began in late January of 2019 and was completed by the end of June 2019. The payload and team traveled to White Sands Missile Range on July 7, 2019 to integrate the instrument with the NSROC payload. The entire process of assembling, optically aligning, and characterizing SISTINE for the first launch was accomplished in under six months. Characterization was performed between each launch in the “long tank” to verify suitable operation before shipping the instrument to the field on subsequent launches.

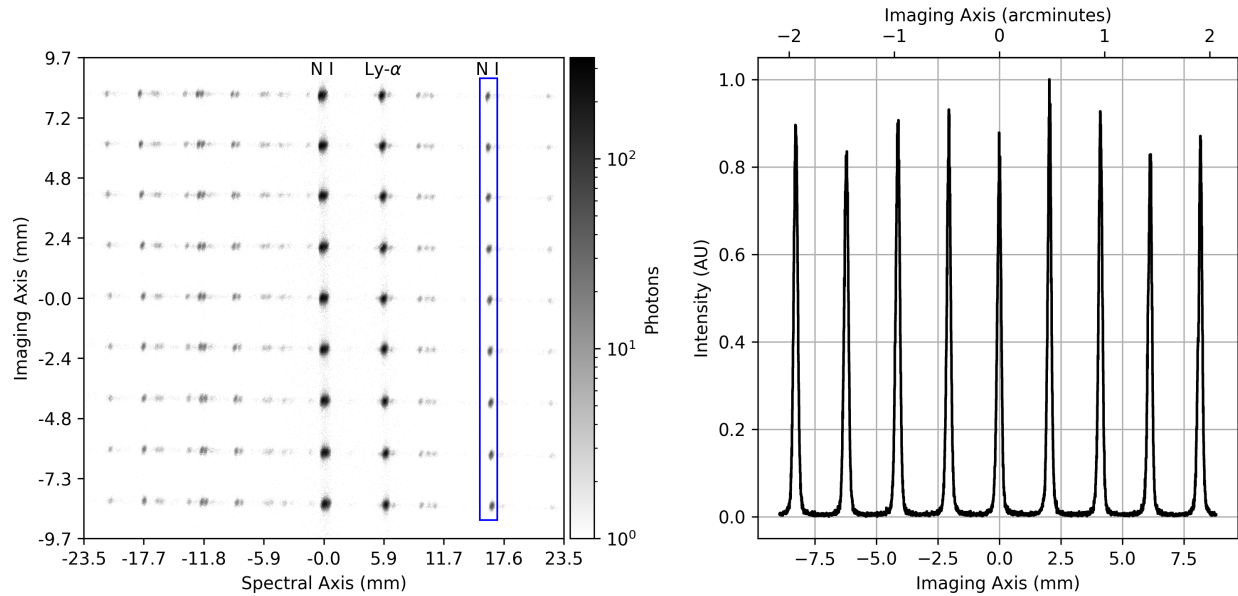


Fig 13: The left plot shows a portion of the SISTINE detector illuminated using a pinhole array to test the imaging capability of the instrument. The wavelength range displayed is roughly 114 – 126 nm. The data in the blue box (N I 124.3 nm) is summed along the spectral axis and displayed in the right plot. The imaging axis maintains telescope limited performance across at least  $\sim 4'$ .

## 5 Flight Performance

SISTINE was launched three times with details summarized in Table 3. The first launch of SISTINE was unable to acquire data due to an experiment misalignment with the payload attitude control system during flight. The ultimate cause of this misalignment was found to be loosening of the primary mirror during vehicle ascent. Minor modifications were made to the mount to better hold the mirror in place during vibration, these modifications are summarized in Section 4.3. The second flight of SISTINE successfully acquired data on target and these results are discussed in detail in Ref. 34. During the second flight of SISTINE, it was found that the telescope thermally defocused during the flight and caused the PSF to be larger than the slit width, limiting the spectral resolving power of the instrument. Modifications to resolve this issue are also discussed in Section 4.3. Target data was acquired during the third flight of SISTINE and optical system performance during that flight was consistent with characterization expectations from the laboratory. These results are discussed in detail in Ref. 35 and in Behr et al. 2024 (in preparation) but also summarized in this work.

Table 3: Summary of SISTINE launches

Mission Number	Launch Date	Launch Site	Target
36.346	August 11, 2019	White Sands Missile Range	NGC 6826
36.373	November 8, 2021	White Sands Missile Range	Procyon A+B
36.339	Jul 6, 2022	Arnhem Space Center	$\alpha$ Centauri A+B

An image of a subset of the detector area centered near Ly $\alpha$  from the third flight of SISTINE

is shown in Figure 14 with imaging and spectral axes labeled. The integration time for this image is 265 s, spanning the on-target exposure time following the real-time pointing adjustment to place the spectrograph slit onto the target stars. The Si III (120.6 nm) line was used to check instrument performance following this flight due to its substantial signal to noise ratio and proximity to the optimized wavelength for SISTINE (120 nm). Figure 15 shows spectral and imaging axis performance for the Si III line. A spectral plot for the  $\alpha$  Cen A Si III line is shown in Figure 15. A Gaussian fit is shown in grey with a FWHM of 0.081 nm and thus a resolving power of 1488. Figure 15 shows an imaging axis plot of the Si III lines for  $\alpha$  Cen A+B. Both stars have Gaussian fits shown in grey and are clearly resolved. The FWHMs for  $\alpha$  Cen A+B are 1.88'' and 1.78'' respectively with a separation of 7.38''. Measurements across other points in the spectrum are consistent with the results shown from Si III and the performance in flight is consistent with characterization efforts from the lab.

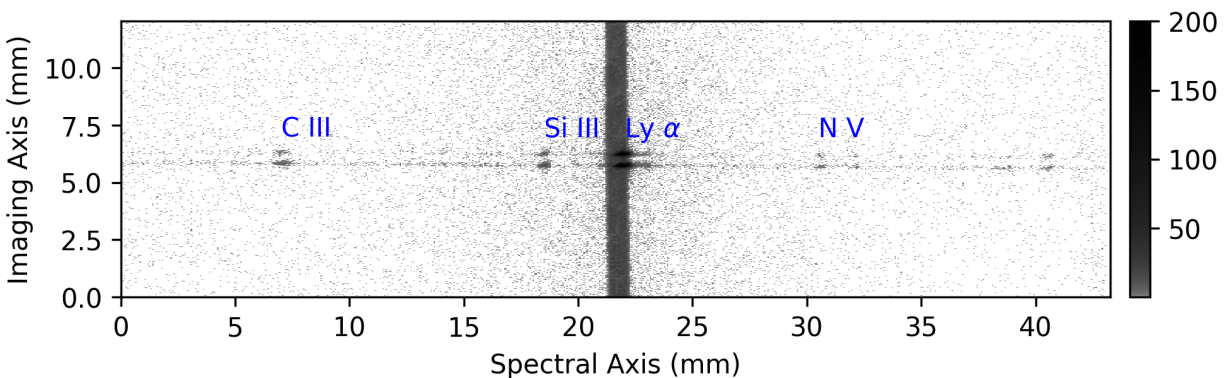


Fig 14: A subset of raw detector data from the SISTINE observation of  $\alpha$  Cen A+B centered near  $\text{Ly}\alpha$ . Both stars are clearly resolved with  $\alpha$  Cen B as the upper spectrum and  $\alpha$  Cen A as the lower spectrum. The large vertical feature located near 22 mm on the spectral axis is  $\text{Ly}\alpha$  airglow fully illuminating the slit. Features visible in the slit airglow image are MCP multifiber boundaries and QE grid shadows, this data has not been flat fielded to remove these features. The spectral axis spans from roughly 116 to 127 nm in wavelength and the imaging axis spans approximately 2.8' in angular extent. Notable spectral features are labeled in blue.

Target acquisition for SISTINE 3 was particularly important due to the orbit of  $\alpha$  Cen A+B and the timescales on which those positions on sky change. Because the slit size of SISTINE is only 10'', both the proper motion and angle of the stars relative to the slit need to be well understood in order to properly point the instrument in flight to maximize separation of the stars along the imaging axis. Observation efficiency on a sounding rocket flight is critical due to the small amount of available observing time ( $\sim 330$  s for SISTINE-3). Observation efficiency is optimized by planning a good initial on-sky orientation to minimize pointing adjustments required during the available observing time. Orbital parameters from Ref. 40 were used to propagate the locations of  $\alpha$  Cen A+B to the predicted launch night time. Results of this predicted propagation are shown in Figure 16. This method was verified against Chandra X-ray Observatory images of  $\alpha$  Cen A+B from 2005 and 2016.<sup>41</sup> The angular orientation in flight was consistent with the predictions. In flight, only fine adjustments were made to the position of the slit on sky but the instrument roll angle was not adjusted. The predicted separation was 7.12'', a 0.26'' difference from the measured separation from flight data. It has come to our attention that a recent publication with

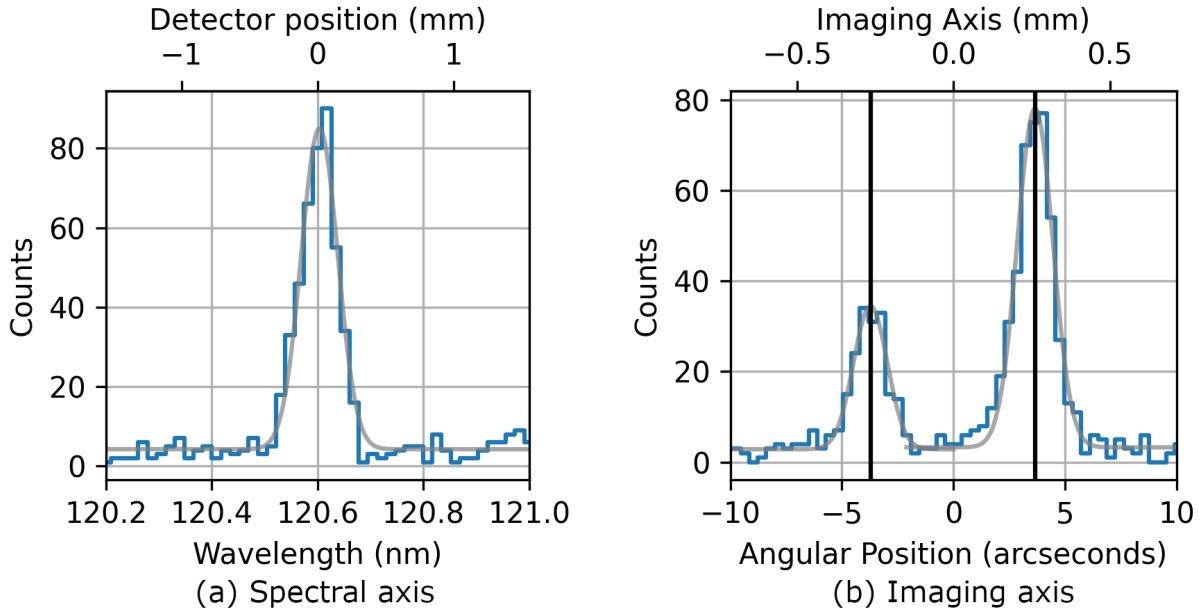


Fig 15: This figure shows flight data from SISTINE-3 in blue and Gaussian fits to this data in grey. Panel (a) shows a plot of the spectrum of the Si III line for  $\alpha$  Cen A with a fit FWHM of 0.081 nm. Panel (b) shows a one dimensional plot along the imaging axis of SISTINE for  $\alpha$  Cen A+B (B the left, A on the right) demonstrating that both stars are well resolved. Gaussian fits produce imaging axis FWHMs of 1.88'' and 1.78'' respectively with a separation of 7.38''.

updated astrometry information was published during the time that SISTINE-3 observations were being planned. Our prediction for angular separation is in agreement with this publication and we find a small difference of 0.81° in position angle.<sup>42</sup>

## 6 Conclusion

SISTINE is a sounding rocket mission designed to probe the FUV radiation environment of nearby stars. SISTINE was launched three times with two of three missions successfully acquiring target data. These flights successfully demonstrated the capabilities of technologies including eLiF, ALD AlF<sub>3</sub> protective layers, and large format ALD processed MCPs. Although SISTINE did not meet all of the goals originally set out, the capability of the instrument to achieve the science goals has been shown along with the capability to handle the launch environment. The overall design worked as intended and would be capable of achieving higher resolving power with suitable time investment on critical aspects of the telescope and spectrograph. Ultimately SISTINE has proven to be a capable FUV imaging spectrograph enabled by significant technology development efforts that are anticipated to be significant for future UV observatories.

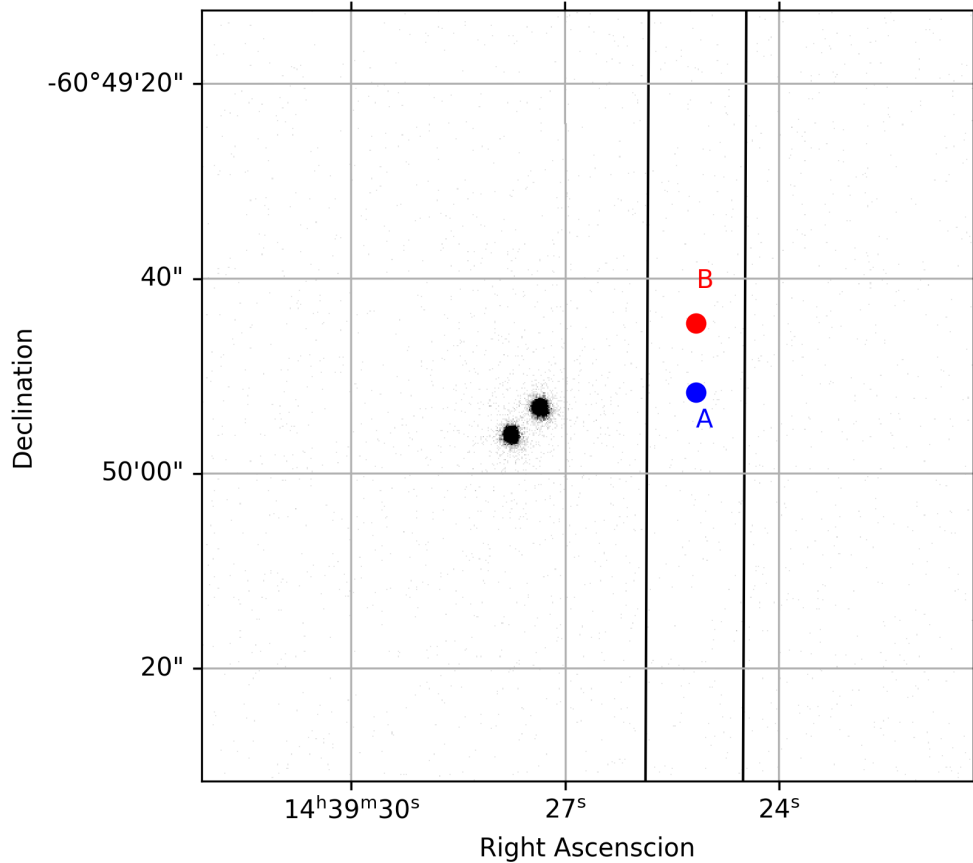


Fig 16: Prediction of the orientation of  $\alpha$  Cen A+B on July 6, 2022.  $\alpha$  Cen A+B is a high proper motion system with an orbit that changes the position angle on-sky appreciably over modest timescales.<sup>40,42</sup> The desired slit orientation on sky is shown in black (note that the full slit length is not shown). The prediction is overplotted on a Chandra X-ray Observatory image from 2016.<sup>41</sup>

#### *Code, Data, and Materials Availability*

The data that support the findings of this paper are not publicly available. They can be requested from the author at [nicholas.nell@lasp.colorado.edu](mailto:nicholas.nell@lasp.colorado.edu).

#### *Acknowledgments*

We thank John Schwenker for inspecting the primary mirror prior to the initial launch. The spatial testing pinholes were fabricated by Alexandra B. Artusio-Glimpse at the National Institute of Standards and Technology (NIST) in the Boulder Microfabrication Facility (BMF) through funding from NIST-on-a-Chip (NOAC). We thank Michael Kaiser, Jarrod Puseman, and Matthew Bridges for their assistance with SISTINE assembly, testing, and support equipment. We acknowledge the hard work and dedication of the NASA Wallops Flight Facility/NSROC payload team, the Physical Sciences Laboratory at New Mexico State University, and the Navy team at WSMR. We thank the NASA Sounding Rockets Program Office, Equatorial Launch Australia, and the Gumatj Corporation for their roles in making the 2022 launch of SISTINE from Australia possible. SISTINE was supported by grant numbers NNX16AG28G and 80NSSC20K0412 from NASA.

## References

- 1 K. France, K. Hoadley, B. T. Fleming, *et al.*, “The SLICE, CHESS, and SISTINE ultraviolet spectrographs: Rocket-borne instrumentation supporting future astrophysics missions,” *Journal of Astronomical Instrumentation* **05**, 1640001 (2016).
- 2 B. T. Fleming, K. France, N. Nell, *et al.*, “SISTINE: a pathfinder for FUV imaging spectroscopy on future NASA astrophysics missions,” in *Space Telescopes and Instrumentation 2016: Ultraviolet to Gamma Ray*, SPIE (2016).
- 3 R. Hu, S. Seager, and W. Bains, “PHOTOCHEMISTRY IN TERRESTRIAL EXOPLANET ATMOSPHERES. i. PHOTOCHEMISTRY MODEL AND BENCHMARK CASES,” *The Astrophysical Journal* **761**, 166 (2012).
- 4 K. France, C. S. Froning, J. L. Linsky, *et al.*, “THE ULTRAVIOLET RADIATION ENVIRONMENT AROUND m DWARF EXOPLANET HOST STARS,” *The Astrophysical Journal* **763**, 149 (2013).
- 5 H. Lammer, F. Selsis, I. Ribas, *et al.*, “Atmospheric loss of exoplanets resulting from stellar x-ray and extreme-ultraviolet heating,” *The Astrophysical Journal* **598**, L121–L124 (2003).
- 6 A. Youngblood, K. France, R. O. P. Loyd, *et al.*, “The MUSCLES Treasury Survey. II. Intrinsic  $LY\alpha$  and Extreme Ultraviolet Spectra of K and M Dwarfs with Exoplanets\*,” *The Astrophysical Journal* **824**, 101 (2016).
- 7 A. Segura, L. M. Walkowicz, V. Meadows, *et al.*, “The effect of a strong stellar flare on the atmospheric chemistry of an earth-like planet orbiting an m dwarf,” *Astrobiology* **10**, 751–771 (2010).
- 8 A. Youngblood, J. S. Pineda, T. Ayres, *et al.*, “Intrinsic  $Ly\alpha$  Profiles of High-velocity G, K, and M Dwarfs,” *ApJ* **926**, 129 (2022).
- 9 J. V. Vallergera and J. B. McPhate, “Optimization of the readout electronics for microchannel plate delay line anodes,” in *Instrumentation for UV/EUV Astronomy and Solar Missions*, S. Fineschi, C. M. Korendyke, O. H. W. Siegmund, *et al.*, Eds., **4139**, 34 – 42, International Society for Optics and Photonics, SPIE (2000).
- 10 O. H. W. Siegmund, T. Curtis, J. B. McPhate, *et al.*, “Development of sealed cross strip readout UV detectors,” in *UV, X-Ray, and Gamma-Ray Space Instrumentation for Astronomy XXII*, O. H. Siegmund, Ed., *Society of Photo-Optical Instrumentation Engineers (SPIE) Conference Series* **11821**, 118210B (2021).
- 11 O. Siegmund, J. McPhate, J. Vallergera, *et al.*, “Development of planacon tubes with cross strip readouts and atomic layer mcps,” in *2020 IEEE Nuclear Science Symposium and Medical Imaging Conference (NSS/MIC)*, 1–6 (2020).
- 12 C. Ertley, O. Siegmund, T. Cremer, *et al.*, “Performance studies of atomic layer deposited microchannel plate electron multipliers,” *Nuclear Instruments and Methods in Physics Research A* **912**, 75–77 (2018).
- 13 C. Ertley, O. H. W. Siegmund, J. Schwarz, *et al.*, “Characterization of borosilicate microchannel plates functionalized by atomic layer deposition,” in *UV, X-Ray, and Gamma-Ray Space Instrumentation for Astronomy XIX*, O. H. Siegmund, Ed., SPIE (2015).
- 14 M. A. Popecki, B. Adams, C. A. Craven, *et al.*, “Microchannel plate fabrication using glass capillary arrays with atomic layer deposition films for resistance and gain,” *Journal of Geophysical Research: Space Physics* **121**(8), 7449–7460 (2016).

- 15 J. V. Vallerga, J. B. McPhate, A. P. Martin, *et al.*, “HST-COS far-ultraviolet detector: final ground calibration,” in *UV/EUV and Visible Space Instrumentation for Astronomy and Solar Physics*, O. H. Siegmund, S. Fineschi, and M. A. Gummin, Eds., *Society of Photo-Optical Instrumentation Engineers (SPIE) Conference Series* **4498**, 141–151 (2001).
- 16 O. H. W. Siegmund, J. McPhate, T. Curtis, *et al.*, “Ultraviolet imaging detectors for the GOLD mission,” in *Space Telescopes and Instrumentation 2016: Ultraviolet to Gamma Ray*, J.-W. A. den Herder, T. Takahashi, and M. Bautz, Eds., *Society of Photo-Optical Instrumentation Engineers (SPIE) Conference Series* **9905**, 99050D (2016).
- 17 B. T. Fleming, M. A. Quijada, K. France, *et al.*, “New UV instrumentation enabled by enhanced broadband reflectivity lithium fluoride coatings,” in *UV, X-Ray, and Gamma-Ray Space Instrumentation for Astronomy XIX*, O. H. Siegmund, Ed., *Society of Photo-Optical Instrumentation Engineers (SPIE) Conference Series* **9601**, 96010R (2015).
- 18 B. Fleming, M. Quijada, J. Hennessy, *et al.*, “Advanced environmentally resistant lithium fluoride mirror coatings for the next generation of broadband space observatories,” *Appl. Opt.* **56**, 9941–9950 (2017).
- 19 C. M. Oliveira, K. Retherford, S. J. Conard, *et al.*, “Aging studies of LiF-coated optics for use in the far ultraviolet,” in *EUV, X-Ray, and Gamma-Ray Instrumentation for Astronomy X*, O. H. Siegmund and K. A. Flanagan, Eds., *Society of Photo-Optical Instrumentation Engineers (SPIE) Conference Series* **3765**, 52–60 (1999).
- 20 V. Dauer, “Optical constants of lithium fluoride thin films in the far ultraviolet,” *Journal of the Optical Society of America B Optical Physics* **17**, 300–303 (2000).
- 21 J. J. Hennessy, K. Balasubramanian, C. S. Moore, *et al.*, “Performance and prospects of far ultraviolet aluminum mirrors protected by atomic layer deposition,” *Journal of Astronomical Telescopes, Instruments, and Systems* **2**(4), 1 – 9 (2016).
- 22 E. G. Loewen, “Replication Of Mirrors And Diffraction Gratings,” in *Optical Surface Technology*, H. Walter, Ed., **0381**, 88 – 104, International Society for Optics and Photonics, SPIE (1983).
- 23 L. Rodríguez-de Marcos, B. Fleming, J. Hennessy, *et al.*, “Advanced Al/eLiF mirrors for the SPRITE CubeSat,” in *Society of Photo-Optical Instrumentation Engineers (SPIE) Conference Series*, *Society of Photo-Optical Instrumentation Engineers (SPIE) Conference Series* **12188**, 1218820 (2022).
- 24 M. A. Quijada, J. del Hoyo, D. R. Boris, *et al.*, “Improved mirror coatings for use in the Lyman Ultraviolet to enhance astronomical instrument capabilities,” in *Society of Photo-Optical Instrumentation Engineers (SPIE) Conference Series*, H. A. MacEwen and J. B. Breckinridge, Eds., *Society of Photo-Optical Instrumentation Engineers (SPIE) Conference Series* **10398**, 103980Z (2017).
- 25 M. A. Quijada, L. V. Rodríguez de Marcos, J. G. Del Hoyo, *et al.*, “Advanced Al mirrors protected with LiF overcoat to realize stable mirror coatings for astronomical telescopes,” in *Society of Photo-Optical Instrumentation Engineers (SPIE) Conference Series*, *Society of Photo-Optical Instrumentation Engineers (SPIE) Conference Series* **12188**, 121881V (2022).
- 26 D. L. Windt and W. Cash, “The soft X-ray/EUV calibration facility at the University of Colorado,” in *X-ray calibration: Techniques, sources, and detectors*, *Society of Photo-Optical Instrumentation Engineers (SPIE) Conference Series* **689**, 167–177 (1986).



- 27 D. L. Windt, J. Cash, Webster C., M. Scott, *et al.*, “Optical constants for thin films of Ti, Zr, Nb, Mo, Ru, Rh, Pd, Ag, Hf, Ta, W, Re, Ir, Os, Pt, and Au from 24 Å to 1216 Å,” *Appl. Opt.* **27**, 246–278 (1988).
- 28 D. L. Windt, J. Cash, Webster C., M. Scott, *et al.*, “Optical constants for thin films of C, diamond, Al, Si, and CVD SiC from 24 Å to 1216 Å,” *Appl. Opt.* **27**, 279–295 (1988).
- 29 N. Kruczek, D. M. Miles, B. Fleming, *et al.*, “High efficiency echelle gratings for the far ultraviolet,” *Appl. Opt.* **61**, 6430 (2022).
- 30 F. Paresce, S. Kumar, and C. S. Bowyer, “Continuous discharge line source for the extreme ultraviolet,” *Appl. Opt.* **10**, 1904–1908 (1971).
- 31 T. A. Cook, W. Cash, and J. C. Green, “Far ultraviolet spectrophotometry of BD +28 4211,” *Advances in Space Research* **11**, 29–32 (1991).
- 32 W. H. Steel, “The autostigmatic microscope,” *Optics and Lasers in Engineering* **4**, 217–227 (1983).
- 33 R. E. Parks and W. P. Kuhn, “Optical alignment using the Point Source Microscope,” in *Optomechanics 2005*, A. E. Hatheway, Ed., *Society of Photo-Optical Instrumentation Engineers (SPIE) Conference Series* **5877**, 102–116 (2005).
- 34 F. C. Aguirre, K. France, N. Nell, *et al.*, “The radiation environments of middle-aged f-type stars,” *The Astrophysical Journal* **956**, 79 (2023).
- 35 P. R. Behr, N. Nell, N. E. Kruczek, *et al.*, “The SISTINE-3 sounding rocket payload: calibration and in-flight performance,” in *UV, X-Ray, and Gamma-Ray Space Instrumentation for Astronomy XXIII*, O. H. Siegmund and K. Hoadley, Eds., **12678**, 1267805, International Society for Optics and Photonics, SPIE (2023).
- 36 K. Hoadley, K. France, N. Nell, *et al.*, “The assembly, calibration, and preliminary results from the Colorado high-resolution Echelle stellar spectrograph (CHESS),” in *Space Telescopes and Instrumentation 2014: Ultraviolet to Gamma Ray*, T. Takahashi, J.-W. A. den Herder, and M. Bautz, Eds., **9144**, 31 – 47, International Society for Optics and Photonics, SPIE (2014).
- 37 N. Kruczek, N. Nell, K. France, *et al.*, “The fourth flight of CHESS: spectral resolution enhancements for high-resolution FUV spectroscopy,” in *Space Telescopes and Instrumentation 2018: Ultraviolet to Gamma Ray*, J.-W. A. den Herder, S. Nikzad, and K. Nakazawa, Eds., **10699**, 100 – 119, International Society for Optics and Photonics, SPIE (2018).
- 38 E. Wilkinson, J. C. Green, S. N. Osterman, *et al.*, “Integration, alignment, and initial performance results of the Far Ultraviolet Spectroscopic Explorer (FUSE) spectrograph,” in *Space Telescopes and Instruments V*, P. Y. Bely and J. B. Breckinridge, Eds., *Society of Photo-Optical Instrumentation Engineers (SPIE) Conference Series* **3356**, 18–29 (1998).
- 39 C. Oliveira, S. Beland, C. T. Keyes, *et al.*, “Wavelength Calibration of the Cosmic Origins Spectrograph,” in *Hubble after SM4. Preparing JWST*, 45 (2010).
- 40 D. Pourbaix and H. M. J. Boffin, “Parallax and masses of  $\alpha$  Centauri revisited,” *A&A* **586**, A90 (2016).
- 41 T. R. Ayres, “The Ups and Downs of  $\alpha$  Centauri,” *AJ* **147**, 59 (2014).
- 42 R. Akeson, C. Beichman, P. Kervella, *et al.*, “Precision millimeter astrometry of the  $\alpha$  centauri ab system,” *The Astronomical Journal* **162**, 14 (2021).